Vortex deformation and turbulent energy of polymer solution in a two-dimensional turbulent flow

Hidema, Ruri
Fukushima, Kengo
Yoshida, Ryohei
Suzuki, Hiroshi

(Citation)
Journal of Non-Newtonian Fluid Mechanics,285:104385

(Issue Date)
2020-11

(Resource Type)
journal article

(Version)
Accepted Manuscript

(URL)
https://hdl.handle.net/20.500.14094/90007660

Vortex deformation and turbulent energy of polymer solution in a two-dimensional turbulent flow

Ruri Hidema*, Kengo Fukushima, Ryohei Yoshida, Hiroshi Suzuki

Department of Chemical Science and Engineering, Kobe University, Kobe 657-8501, Japan

*Corresponding Author
Phone: +81-78-803-6657
Fax: +81-78-803-6657
hidema@port.kobe-u.ac.jp

An experimental study was performed to investigate the effects of the extensional rheological properties of polymer solutions on vortex deformation in turbulent flow and turbulent statistics. To focus on the extensional properties, a self-standing two-dimensional (2D) turbulent flow was used as an experimental setup, and the flow was observed through interference patterns and particle image velocimetry (PIV). Vortex shedding and the resulting deformation in the 2D flow were categorized into three types. The vortex flow regime was defined by the shedding frequency and relaxation time of the polymer solution. Turbulent energy was suppressed by polymer additives; however, a characteristic peak reappeared with increasing concentration. The results imply that the characteristic turbulent energy peak is influenced by the relaxation process of the extended polymers in the flow.

Keywords: Extensional rheological properties, Relaxation time, Two-dimensional turbulent flow, Vortex shedding, Turbulent statistics

1. Introduction

The addition of a small amount of polymer to a Newtonian fluid reduces the frictional drag of the flow and delays the transition to turbulent flow. To understand the drag reduction phenomenon, many experimental and numerical studies have been conducted in the past decades [1–6]. An important feature of this phenomenon is the anisotropic effect, which is due to the polymer extension in the flow [7–10]. The extension of polymers, caused by the polymer coil-stretch transition, influences the flow, that is, it modifies energy transportation in the flow. To describe the subsequent onset of drag reduction to the coil-stretch transition, Min et al. [11] adopted the elastic theory on the transport equations for kinetic and elastic energy.

Kinetic energy is transported through the elastic energy created by the polymer extension at the wall in a turbulent flow. Thus, the polymer extension estimated from the Weissenberg number and the time criterion, such as the relaxation time, is an important parameter that influences energy transportation. Min et al. [11] suggested that the relaxation time of a polymer should be sufficiently long to transport the elastic energy from the near-wall region to the buffer or log layer. The influence of the polymer extension and relaxation time of fluids on the turbulent drag reduction has also been demonstrated in other experimental studies [12–14]. An important consensus among researches in these previous studies has been that drag reduction occurs as a consequence of the dynamic interaction between polymer molecules and turbulence only when the polymer relaxation time becomes comparable to the characteristic time-scale of the flow [12]. It became possible to conduct quantitative experimental analysis, especially after the development of the capillary break-up extensional rheometer (CaBER). Owolabi et al. [12] proposed an equation to formulate the drag reduction efficiency in terms of polymer extension based on the Weissenberg number, which is calculated using the relaxation time measured by a CaBER.

Polymer extension and spatiotemporal non-uniform turbulent drag reduction have become popular areas of research in recent numerical studies. Turbulent flows are extensional, and the straining motion of the fluids, which is caused by an extensional flow, overcomes the rotation of the fluids, thereby stretching the polymers to their fully extended length. Xi and Graham, and the following related works, revealed that a highly extended polymer induces the intermittent dynamics of Newtonian and viscoelastic turbulence near the wall [15–17]. A minimal flow unit at the wall is laminarized by extended polymers and modified larger domains. Indeed, the instantaneous degree of polymer stretching and drag reduction are temporally anti-correlated. The polymers stretch in active turbulence and induce a subsequent hibernation period, that is, a weak turbulent flow. During the hibernation period, the drag is low, and the polymers relax [18–21].

Another approach to comprehend the turbulent flow dynamics influenced by the rheological properties of the fluids is to study vortex shedding from a cylinder in viscoelastic fluids. Cadot [22] suggested that anisotropic vortex deformation at a cylinder in viscoelastic fluids appeared to be similar to what is

observed in turbulence, and thus, could lead to a better comprehension of vortex inhibition and drag reduction. Therefore, numerous experimental and numerical studies on visualizing vortex shedding at a cylinder have been conducted [22–30]. Usui et al. first proposed that the Strouhal number of vortex shedding in a viscoelastic solution was correlated to the Weissenberg number [24]. Cadot et al. mentioned that the shear viscosity of a polymer solution only marginally influences vortex shedding; conversely, the elastic properties of the solution influence the vortex shedding frequency and the formation length [22]. Here, the formation length is the distance required to form vortices from the cylinder surface. It has been suggested that when the relaxation time related to the elasticity approaches the diffusive time scale in the fluids, the stabilization mechanism of vortex shedding occurs. Here, again, the time criterion is important for the formation and stability of the vortices. Coelho and Pinho studied the effects of elasticity and shear thinning on the Strouhal number of vortex shedding [27]. They suggested that the Strouhal number decreases by elasticity and increases by shear thinning. In these studies, the Reynolds numbers of the flows were relatively low, that is, approximately 50.

In recent studies on vortex shedding at a cylinder in viscoelastic fluids, numerical studies have achieved higher Reynolds numbers, and it has been revealed that viscoelastic fluids induce drag enhancement and drag reduction [31, 32]. These two regimes, drag enhancement and drag reduction, are influenced by the Weissenberg number and Reynolds number. The addition of polymers varied the velocity fields, vortex shedding, and local elongation of the fluid elements [32], which implies the extension of the polymers around the cylinder. Relatively recently, drag enhancement and the extension of the polymers around the cylinder have been experimentally investigated by visualizing fluorescently stained deoxyribonucleic acid (DNA) [33]. Moreover, polymer elongation around a cylinder was observed in a recent numerical study with molecular dynamics simulation [34]. These results again confirmed that the extended polymer effects on drag reduction are not linear.

To focus on the extensional stress and polymer extension in a flow, a two-dimensional (2D) flow is useful [35, 36]. A self-standing flowing soap film is an example of a 2D flow, where the flow surface is a free surface [37]. Thus, the flowing soap film is relatively free from shear stress at the wall. When a comb of equally spaced cylinders is inserted into the flow, vortices are generated at each

cylinder, and the vortices merge with each other to develop a turbulent flow downstream. The extensional flow appears around each cylinder, and thus, the vortices in the flow are influenced by the extensional rheological properties of the fluids [38–40].

In our previous studies, we focused on the effects of the extensional rheological properties of polymer solutions on the modification of turbulent flow in a 2D flow [41]. In one of these studies, we investigated whether vortex shedding at a comb is influenced by the relaxation time of the fluids, as measured by a CaBER. Vortex shedding was categorized into three types, and the vortex deformation altered the 2D turbulent flow. In this study, extensional rates at the comb are varied by changing the spacing between the cylinders, and how that influences vortex shedding of the polymer-doped 2D flow is tested. Here, the extensional rate is represented by a mean value, as mentioned in Section 2.2, which induces the succeeding changes in the 2D turbulent flow. The 2D turbulent flow statistics are measured and analyzed by the particle image velocimetry (PIV) method. The energy transfer in the 2D flow of the polymer solution is precisely analyzed by the turbulent flow statistics, and we discuss the characteristic energy peak appearing behind a cylinder in the polymer-doped 2D flow.

2. Experimental Procedures

2.1. Measurement of material and rheological properties

Sodium dodecylbenzenesulfonate (SDBS) was dissolved in ultrapure water at a concentration of 2 wt%. Polyethyleneoxide (PEO, molecular weight: 3.5×10^6) was used as a drag-reducing flexible polymer, and the solution concentrations were varied from 0.25 to 1.5×10^{-3} wt%. The overlap concentration of PEO was approximately 1.2×10^{-2} wt%.

The viscosity of the sample solutions was measured using a rheometer (MCR301: Anton Paar) with a cone-plate device at shear rates from 1 to 1000 s^{-1}. The relaxation time of the sample solutions under extensional stress was measured using a CaBER (Thermo Scientific) [42–44]. The extensional property of the sample solutions was evaluated by the relaxation time. The diameter of the end plate of the CaBER was 6 mm, the initial distance between two end plates was set as 3

mm, and the final distance between the two plates was adjusted to 8 mm. The diameter of the neck of the liquid column, D [mm], was plotted relative to time, t [s]. The thinning process of the diameter in the elasto-capillary region was fit using the fitting function, $D = A\exp(-t / 3\lambda)$, to calculate each relaxation time under extensional stress, λ [s], of each sample solution. Here, A [m] is a constant that was determined by the experiment.

2.2. Experimental apparatus used to create flowing soap films.

The experiments were performed using the apparatus displayed in Fig. 1. A complete image of the flowing soap film as a 2D flow is presented in Fig. 1(a). The details of the apparatus are provided elsewhere [41]. The flow rate, Q [L/s], measured by a flowmeter (KEYENCE, FD-SF1) was maintained constant at 25 mL/min. As the flow was gravity-driven, the velocity achieved a constant value of approximately 300 mm behind the injection nozzle [37]. The streamwise mean velocity, U_m [m/s], obtained by the PIV, was approximately 1.5 m/s when the flow rate was 25 mL/min. The mean thickness of the water layer, h [m], was approximately 3.5 μm.

To create a 2D turbulent flow on the flowing soap films, a comb composed of equally spaced cylinders was inserted perpendicular to the flow 130 mm downstream from the beginning of the parallel section in the channel. The diameter of the cylinder, d [m], was 3 mm. The Reynolds number as calculated by the U_m, solution viscosity, diameter of the cylinder, and solution density was approximately 4,600. The cross-sectional area of the water layer decreased at the comb, which induced an increase in the local velocity around the comb. The increase in the local velocity induced an extensional rate. The extensional rate occurred around a cylinder with a certain distribution [33]. Here, the mean value of the extensional rate, $\dot{\varepsilon}$ [s^{-1}], was calculated by $S(t) = S_0\exp(-\dot{\varepsilon}t)$ to represent the flow condition, where S_0 [m^2] is the cross-sectional area of the water layer before deformation, $S(t)$ [m^2] is the cross-sectional area after deformation, and t [s] is the time required for the deformation from S_0 to $S(t)$ [41]. The mean extensional rate was varied by changing the flow rates and spacing between the centers of the cylinders. In the present study, the flow rate and diameter of the cylinder were constant. The spacing of the column was varied as 9, 12, and 15 mm; thus, the

approximate $\dot{\varepsilon}$ was calculated to be 220, 290, and 400 s^{-1} for the respective spacings. This $\dot{\varepsilon}$ influences the rheological properties of the polymer solution.

We observed the flow at two positions using two methods. The first observed area was labelled Test section 1; it was from immediately under the comb to 50 mm downstream with a 45 mm width. The second observed area was labelled Test section 2; it was from 150 mm downstream from the comb to 200 mm downstream with a width of 45 mm (Fig. 1(c)). The precise method for observing the flow is described in the following sections.

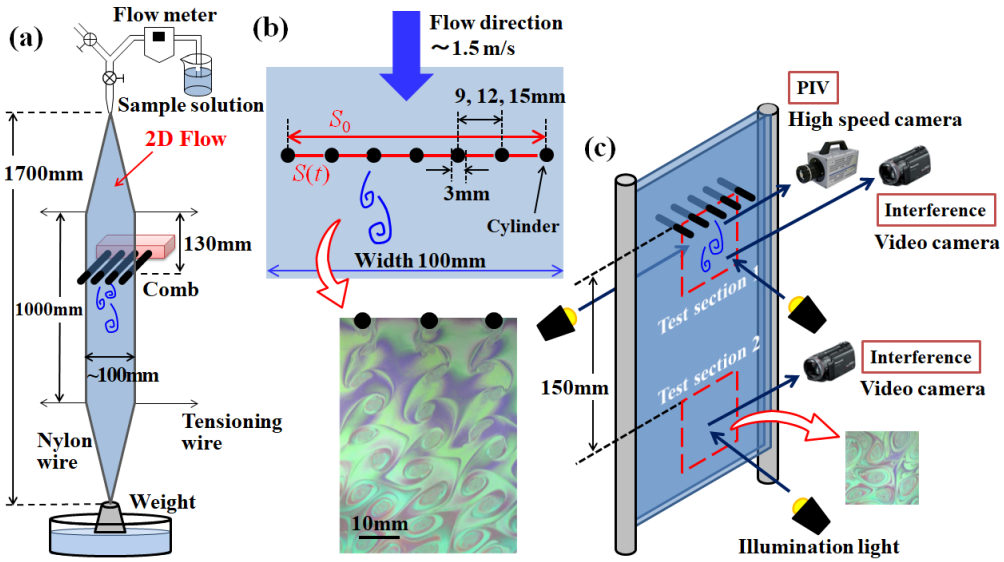

Fig. 1 Schematic of experimental apparatus.

2.4. Visualization of flow by interference patterns and single image analysis

Vortex shedding at the comb, and 2D turbulent flow that is a consequence of the merged vortices downstream, were observed in Test sections 1 and 2 through interference patterns of the film. The interference patterns contain information on the thickness of the water layer in the 2D flow. The vortices observed through the interference patterns in Test section 1 correspond to the vorticity of the flow [41, 45]. Here, we used a commercial white light (Toshiba, EFA25EN/22) to illuminate the flow. Then, the interference images of the flow were recorded by a digital video camera (Panasonic TM700) in the test sections. The shutter speed of the video camera was set at 1/3,000 s. The time interval for a series of images was adjusted to 1/60 s. Each recorded camera frame was converted into a file with an RGB value

of 0–255 and a spatial resolution of 640 × 360 pixels, which corresponds to 42 × 23 mm^2.

Because the thickness fluctuation is considered as a passive scalar in the 2D flow, the interference patterns were used to calculate the power spectrum of the passive scalar in the flow. Part of the image, 256 × 256 pixels, was clipped from a still image recorded in Test section 2. The clipped image was analyzed by 2D fast Fourier transform to obtain a power spectrum, $<I^2(k_x, k_y)>$, of the image. The power spectrum, $<I^2(k_x, k_y)>$, was calculated based on the green RGB pixel intensity, G, with a Hamming window where k_x m^{-1} and k_y m^{-1} denote the spatial wavenumber in the streamwise and normal directions in the interference image, respectively. The green RGB pixel intensity, G, was selected to avoid variation in the order of interference in the data acquisition area [38–41]. The power spectrum exhibits scaling behavior as $<I^2(k_x, k_y)> \sim k_x^{\alpha}$ and $<I^2(k_x, k_y)> \sim k_y^{\beta}$ in the streamwise and normal directions, respectively. The scaling index of the power spectrum is influenced by the energy transfer in the 2D flow; α and β are informative for evaluating the energy transfer in a 2D flow, which varies by polymer additive [38–41].

2.5. Velocity fields measured using PIV and turbulent statistics analysis

To obtain precise information of the vortices and 2D turbulent flow, the velocity fields in Test section 1 were measured by PIV. The local flow fields fluctuate around the grids and gradually approach a steady mean flow with an increase in the distance from the comb. Therefore, only Test section 1 was measured using PIV. Polystyrene particles with a diameter of 2.11 μm were seeded at a concentration of 1.12 × 10^{-2} vol% as tracer particles for PIV measurements. To visualize the tracer particle trajectories around the grid, a mercury lamp and two halogen lamps as bright light sources were set behind the flowing soap films. A high-speed video camera (Photoron, FASTCAM SA3) was set in front of the soap film, as indicated in Fig. 1(c). The shutter speed of the video camera was 1/10,000 s, and the time interval between two frames was adjusted to 1/3,200 s. The frame rates of the high-speed camera to obtain the velocity fields were 3200 fps.

Commercial software (LaVision, DaVis8) was employed to calculate the velocity fields from a series of images (Fig. 9). Each frame had 512 × 480 pixels, corresponding to 33.2 × 31.2 mm. The interrogation window size to calculate the velocity fields was 8 × 8 pixels, and the overlap percentage of each window was 50%. Based on the local velocity, the turbulent energy, k [m^2/s^2], was calculated using Eq. (1).

$$k = \frac{\overline{u_\iota u_\iota}}{2} \tag{1}$$

Here, u_i [m/s] is the local velocity fluctuation, as indicated in, $u_i = U_i - \overline{U}_i$, where $\overline{U}_i$ [m/s] indicates the mean local velocities in the streamwise and normal directions, and U_i [m/s] indicates the local instantaneous velocities in the streamwise and normal directions.

Eq. (2) displays the transport equation for k.

$$\frac{\partial k}{\partial t} + \overline{U_i}\frac{\partial k}{\partial x_i} = P + D - \varepsilon, \tag{2}$$

where P [m^2/s^3] is the production, D [m^2/s^3] is the diffusion, and ε [m^2/s^3] is the dissipation of the turbulent energy. ∂x_i is the distance between the velocity grids in the streamwise and normal directions. In Eq. (2), in the case of Newtonian fluids, P, D, and ε are calculated by Eqs. (3)–(5).

$$P = -\overline{u_\iota u_j}\frac{\overline{\partial U_\iota}}{\partial x_j} \tag{3}$$

$$D = -\frac{\partial}{\partial x_j}\left(\frac{1}{\rho}\overline{u_j p} + \frac{1}{2}\overline{u_\iota u_\iota u_j} - \nu\frac{\partial k}{\partial x_j}\right) \tag{4}$$

$$\varepsilon = \nu\overline{\frac{\partial u_\iota}{\partial x_j}\frac{\partial u_\iota}{\partial x_j}} \tag{5}$$

Here, ν [m^2/s] is the kinematic viscosity. However, in the present study, the first term on the right-hand side of Eq. (4) was not included in the calculations. This is because of the following three reasons: it is difficult to measure the accurate 2D flow pressure fluctuation, p [Pa], by using the velocity vector obtained in the present study because both sides of the 2D flow were exposed to atmospheric pressure, and

the water layer in the 2D flow was extremely thin. Therefore, it is reasonable to consider the pressure fluctuation p in the flow to be negligible. The challenge to obtain p would be our next step. Subsequently, the convection, C [m^2/s^3], of the turbulent energy, and the budget were calculated using Eqs. (6) and (7).

$$\overline{U_i}\frac{\partial k}{\partial x_i} = C \tag{6}$$

$$Budget = P + D - \varepsilon - C \tag{7}$$

Here, Eqs. (2) and (7) present the turbulent energy balance for Newtonian flow. For polymer solutions, additional terms will be present owing to the polymer stress tensor, as shown in Eq. (8) [21].

$$\frac{\partial k}{\partial t} + \overline{U_i}\frac{\partial k}{\partial x_i} + \text{Contribution of polymer stress tensor} = P + D - \varepsilon \tag{8}$$

However, the extra term cannot be directly measured experimentally; therefore, we adopt Eqs. (2) and (7) for both polymer-free and polymer solutions.

To obtain the velocity fields without the incorrect vector, a median vector was computed by the local median filter as a vector post-processing by using a commercial software (LaVision, DaVis8). However, it was not possible to eliminate all the incorrect vector from the velocity fields, especially at the edge of the cylinder. Therefore, to eliminate the missing incorrect vector, the local velocities U_i at a grid that fit to one of the following two cases were determined: the local absolute velocity, $\sqrt{U_i U_i}$, that is greater than 1.67U_m; the *relative velocity* that is a comparison between U_i at the grid and the average velocity of four neighboring grids, $U_{4\text{grids}}$, that is, $\left|U_i - U_{4\text{grids}}\right|$ is greater than 2U_m. These threshold values, such as 1.67 U_m and 2 U_m, were set based on an empirically led value. When U_i fits to one of these cases, U_i is considered as an incorrect velocity and is replaced with $U_{4\text{grids}}$.

3. Results and Discussion

3.1. Rheological properties of sample solutions

The zero shear viscosities, η_0 [mPa·s], and relaxation times, λ [ms], of the sample solutions are listed in Table 1. Specifically, the η_0 of the sample solutions containing PEO was virtually identical to that of the polymer-free solution. Whereas the λ of the polymer-free solution was low, the λ of the PEO solution increased with its concentration. The relaxation time measured with a CaBER represents the extensional rheological properties of the solutions.

Table 1. Rheological properties of sample solutions

		Zero shear viscosity η_0 [mPa·s]	Relaxation time λ [ms]
Polymer free solution		1.08	0.345
PEO Concentration [$\times 10^{-3}$wt%]	0.25	1.09	4.16
	0.50	1.10	7.01
	0.75	1.13	9.78
	1.0	1.12	12.8
	1.25	1.12	15.8
	1.5	1.16	18.9

3.2. Vortex shedding at comb influenced by polymers and extensional rates

In the experiments, vortices were shed at the comb, which was observed in Test section 1; these vortices were advected downstream to produce 2D turbulent flow that was observed in Test section 2. Here, we compare the images of vortex shedding in the polymer-doped flow at several mean extensional rates, $\dot{\varepsilon}$. The extensional rate was varied by the spacing between the grids, as described in Section 2.2. Figs. 2–4 display vortex shedding from a cylinder of the comb in each solution at each $\dot{\varepsilon}$. Here, we capture the wake flow at a single cylinder of the comb. The black circles represent the cylinders of the comb. As can be observed in Fig. 2, for the polymer-free solution, the vortices were produced immediately after the cylinder (Fig. 2(a)). The vortices were gradually enhanced with the distance from the cylinder and merged with other vortices downstream. The wake region behind the cylinder expanded when the PEO concentrations were increased to 0.25 and 0.5

$\times 10^{-3}$ wt%, (Figs. 2(b) and (c)). For these cases, the distance from the cylinder to the position where the vortices were generated shifted downstream. Herein, we call this distance the formation length. We defined these original and marginally deformed vortices observed at concentrations less than 0.5×10^{-3} wt% as Vortex-Type1. Subsequently, for the PEO 0.75×10^{-3} wt% and 1.0×10^{-3} solutions, the vortices diminished in Test section 1 (Figs. 2(d) and (e)), which we defined as Vortex-Type2. However, the vortices appeared again under the cylinder when the concentration of PEO exceeded 1.25×10^{-3} wt%; we defined these as Vortex-Type3. The Vortex-Type3 observed in the relatively high PEO concentration solution was significantly different from the original vortex, Vortex-Type1.

In Figs. 3 and 4, vortex shedding with the comb of the shorter spacing column corresponds to a higher extensional rate. The concentration at which Vortex-Type2 appeared was shifted to a lower concentration when $\dot{\varepsilon}$ was greater. As can be observed in Fig. 4(d), Vortex-Type2 was observed at a PEO concentration of approximately 0.5 0.6×10^{-3} wt%. In addition to the effects of $\dot{\varepsilon}$, we found that the neighbouring vortices shed at the next cylinder enhanced the Vortex-Type3. When virtually the same $\dot{\varepsilon}$ was achieved in the two flows, that is, the wider spacing with the higher velocity, and the shorter spacing with the lower velocity, the results were not the same. The shorter spacing enhanced the Vortex-Type3.

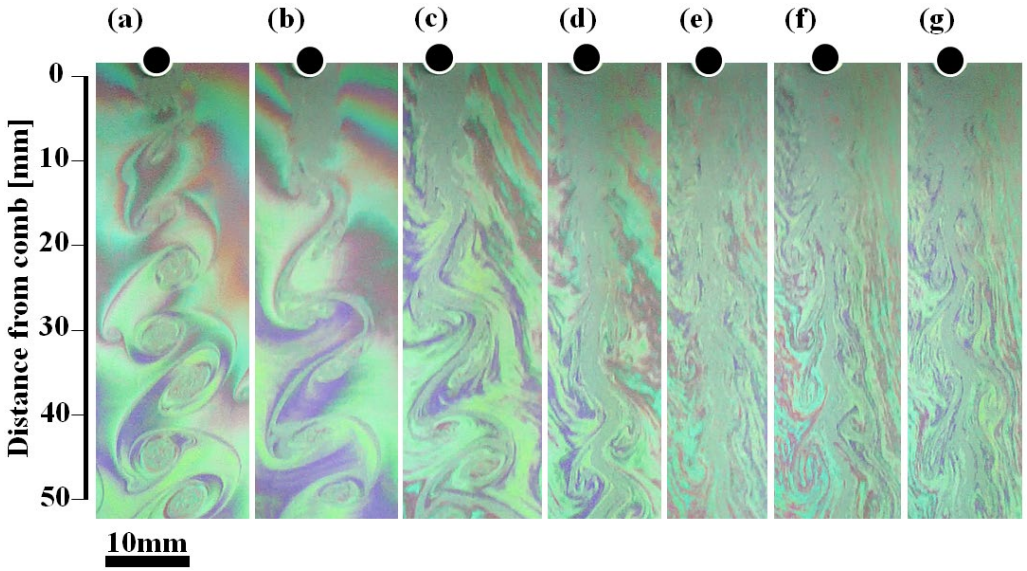

Fig. 2 Interference patterns of vortex shedding in PEO solution at l_s = 15 mm and $\dot{\varepsilon}$ = 220 s^{-1} obtained in Test section 1. (a) Indicates flow of polymer-free solution; (b)–(g) denote flow of PEO solution at concentrations of (b) 0.25, (c) 0.5, (d) 0.75, (e) 1.0, (f) 1.25, and (g) 1.5×10^{-3} wt%, respectively.

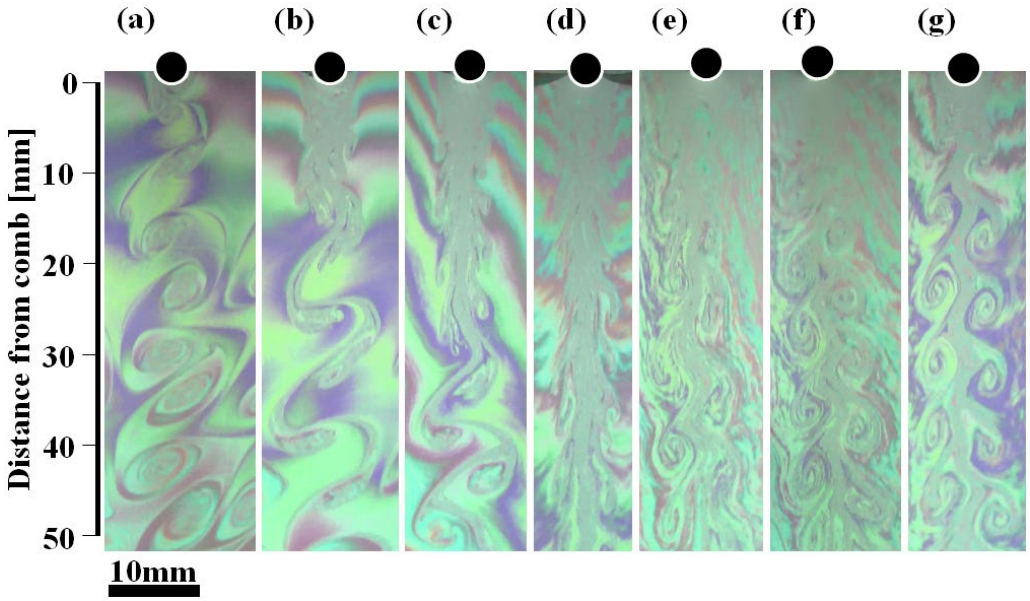

Fig. 3 Interference patterns of vortex shedding in PEO solution at l_s = 12 mm and $\dot{\varepsilon}$ = 290 s^{-1} obtained in Test section 1. (a) Indicates flow of polymer-free solution; (b)–(g) denote flow of PEO solution at concentrations of (b) 0.25, (c) 0.5, (d) 0.75, (e) 1.0, (f) 1.25, and (g) 1.5 × 10^{-3} wt%, respectively.

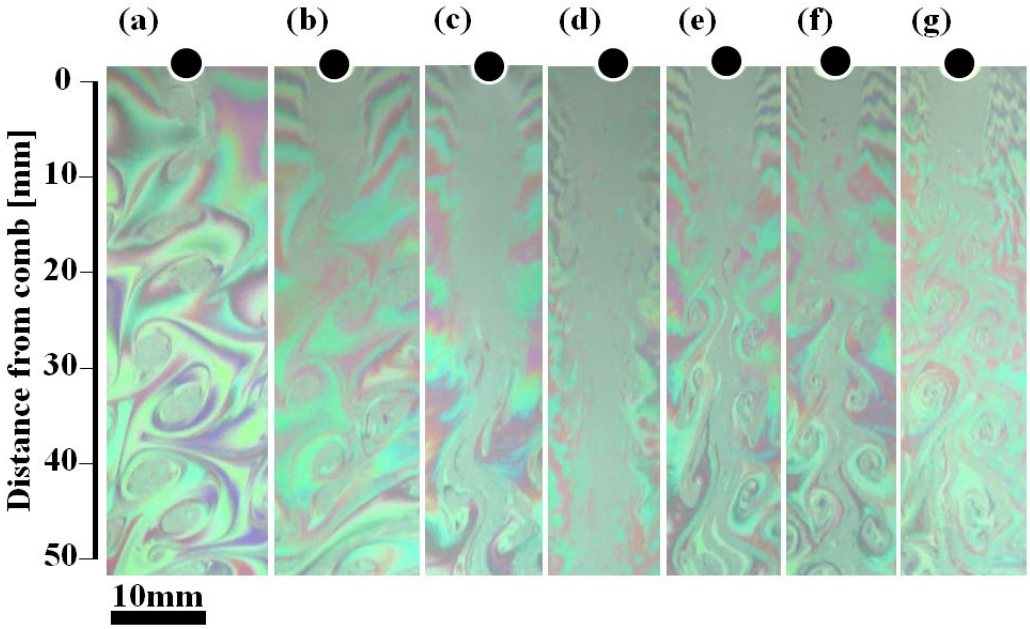

Fig. 4 Interference patterns of vortex shedding in PEO solution at l_s = 9 mm and $\dot{\varepsilon}$ = 400 s^{-1} obtained at Test section 1. (a) Indicates flow of polymer-free solution; (b)–(g) denote flow of PEO solution at concentrations of (b) 0.25, (c) 0.5, (d) 0.6 (e) 0.75, (f) 1.0, and (g) 1.25×10^{-3} wt%, respectively.

3.3. Effects of Rheological properties on vortex shedding

A series of vortices similar to Vortex-Type1, 2, and 3 were suggested in a previous numerical study [32]. In this study, the vortices shed at a single cylinder were deformed and diminished by increasing the Weissenberg number; however, again, another structure appeared at a higher Weissenberg number. Whereas the effects of the rheological properties of the sample solution on vortex shedding and vortex deformation have been discussed in numerous previous studies [26], the variation occurred primarily in the one-way direction. That is, the shear thinning, elasticity, and concentration of the fluids merely increased or decreased the vortex shedding frequency, namely the Strouhal number. Conversely, in the present study, the vortex shedding frequency was decreased, and then the frequency was increased by increasing the polymer concentration of the solution, as suggested by Xiong et al. [32]. To characterize the vortex shedding frequency, the Strouhal number, St [-], of the vortices at each condition was calculated by $St = fd/U_{vortex}$, where f [1/s] is the frequency of vortex shedding obtained by $f = U_{vortex}/L_{vortex}$. Here, U_{vortex} [m/s] is the vortex velocity that is calculated from the distance travelled by the same vortices divided by time, which is obtained by the sequence image clipped from the video. The U_{vortex} was marginally smaller than U_m. L_{vortex} [m] is the distance between two vortices that rotate in the same direction on the same side of the cylinder. As indicated in Fig. 5, the St of the original vortices was approximately 0.2 to 0.25. The St was virtually constant or only marginally increased in the Vortex-Type1 regime; the St marginally decreased in Vortex-Type2, and subsequently St again increased in Vortex-Type3 regime. In the case of the Vortex-Type2 regime, the vortices virtually disappeared in the region close to the comb. However, weak vortices were observed further downstream in Test section 2. Therefore, it was possible to calculate St of Vortex-Type2 based on the observation in Test section 2. The St of Vortex-Type3 reached a higher value than the original vortices. In the case of flow at 400 s^{-1}, the St of Vortex-Type3 marginally decreased at high concentrations. This behavior seemed to be because of the weakening of the vortices again at that concentration. This tendency seemed to be affected by the extensional rate.

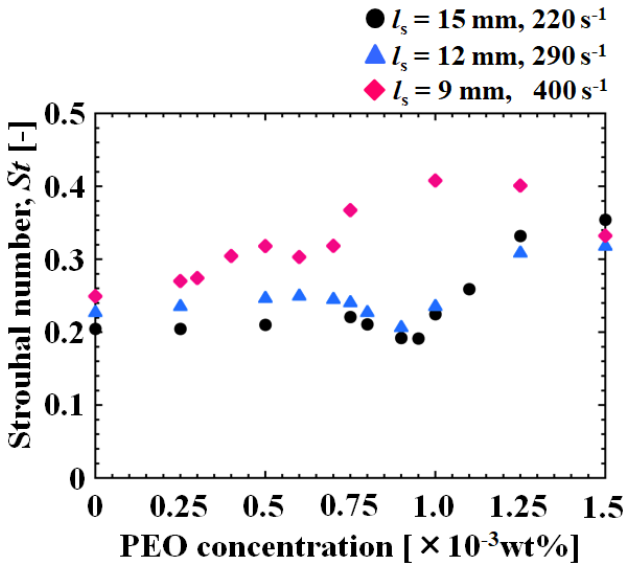

Fig. 5 Strouhal number of vortices at each PEO concentration and spacing, l_s.

To clarify the background mechanism of vortex shedding and deformation, the effect of the rheological property of each solution on the flow was considered. Here, a characteristic time scale of vortex shedding, $1/f$, and that of the extensional solution rheology were compared. The extensional solution rheology was represented by the relaxation time, λ [s], as measured under extensional stress with a CaBER. The λ of each solution and $1/f$ of each flow under different conditions are displayed in Fig. 6. The λ of the solution increased consistently with the PEO concentration. The initial value of $1/f$ was influenced by l_s, and was varied by increasing the PEO concentration, namely the relaxation time, λ. The relationship between $1/f$ and λ influenced vortex shedding and deformation. Vortex-Type1 was observed when $1/f > \lambda$, Vortex-Type2 was observed when $1/f \cong \lambda$, and Vortex-Type3 appeared when $1/f < \lambda$. It appeared that the vortex flow regime was mainly influenced by the relationship. Moreover, in the flow regime of Vortex-Type2, the period of vortex shedding marginally increased with an increase in the relaxation time, λ, that is, a rock-on phenomenon. This occurred for all columns.

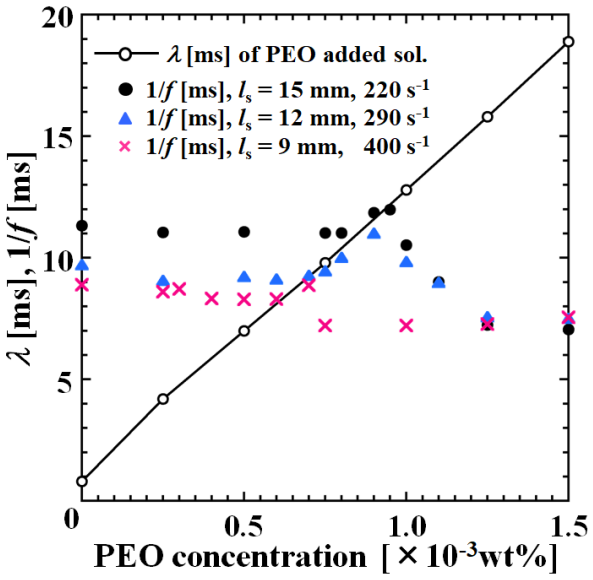

Fig. 6 Relaxation time, λ, and period of vortex shedding, $1/f$, of each comb.

3.4. Laminarization of 2D turbulence with polymer additives

The mean extensional rate at the comb was varied, and the effects of this action on vortex shedding of the polymer-doped 2D flow were verified. The succeeding changes in the 2D turbulent flow were observed. Figure 7 displays the 2D flow at Test section 2, as visualized by the interference patterns. The concentration selected in Fig. 7 is in the region of Vortex-Type1, Vortex-Type2, and Vortex-Type3 at each comb. In the case of the polymer-free solution in the Vortex-Type1 regime, the vortices in the 2D turbulent flow became larger in the downstream region, as indicated in Fig. 7(a), (d), and (g). In the case of the Vortex-Type2 regime, the vortices virtually disappeared in Test section 1; however, the vortices appeared downstream and merged with each other. Conversely, vortices in the flow became longer and thinner in Test section 2, where we observed Vortex-Type3 in Test section 1.

These images were quantified by calculating the power spectrum, $<I^2(k_x, k_y)>$, in both the streamwise and normal directions. The power spectrum exhibits scaling behavior in both directions as $<I^2(k_x)> \sim k_x^{\alpha}$ and $<I^2(k_y)> \sim k_y^{\beta}$. Here, α and β denote the scaling indices in the streamwise and normal directions, respectively. The scaling indices in each direction are indicated in Fig. 8. Both α and β indicate $-5/3$ in the polymer-free solution. This value appears when the flow is dominated by an inverse energy cascade, which is a feature of 2D turbulence [31, 32, 37, 40].

Examples for obtaining the scaling indices with the power spectrum based on the green RGB pixel intensity, G, are provided in our previous studies [40]. The scaling index in the normal direction, β, approached a value of "−1"' asymptotically with increasing PEO concentration. The scaling index in the streamwise direction, α, reached a value of approximately −1.2 with increasing PEO concentration. The scaling index "−1" appears when the inverse energy cascade ceases to exist, and the flow is dominated by the enstrophy cascade. This suggests that the energy transfer in the 2D turbulent flow was influenced by the PEO. Moreover, the effects of the PEO were different in the streamwise and normal directions; that is, the variation was greater in the normal direction. This implies anisotropic energy transfer due to the polymers in 2D flows. We consider that the anisotropy is due to the anisotropic characteristics of the extensional rheology of the polymer solution. Moreover, there is a concentration where the scaling index jumped to a greater value. The discontinuous change occurred at the concentration where Vortex-Type2 was observed in Test section 2. Therefore, the transition concentration was reduced with the comb of the shorter l_s, i.e., the higher $\dot{\varepsilon}$. This result appears reasonable because the anisotropic effects of the extensional rheology are enhanced when $\dot{\varepsilon}$ is greater.

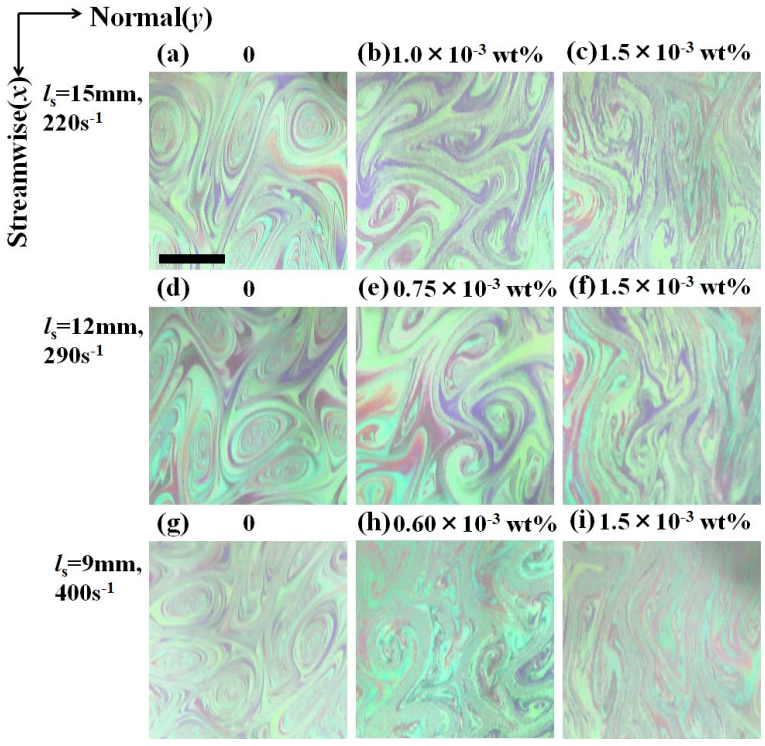

Fig. 7 Interference images of 2D turbulent flow produced with different combs, that is, different extensional rates. Flow regimes in Test section 1 are Vortex-Type1 in (a), (d), and (g); Vortex-Type2 in (b), (e), and (h); and Vortex-Type3 in (c), (f), and (i).

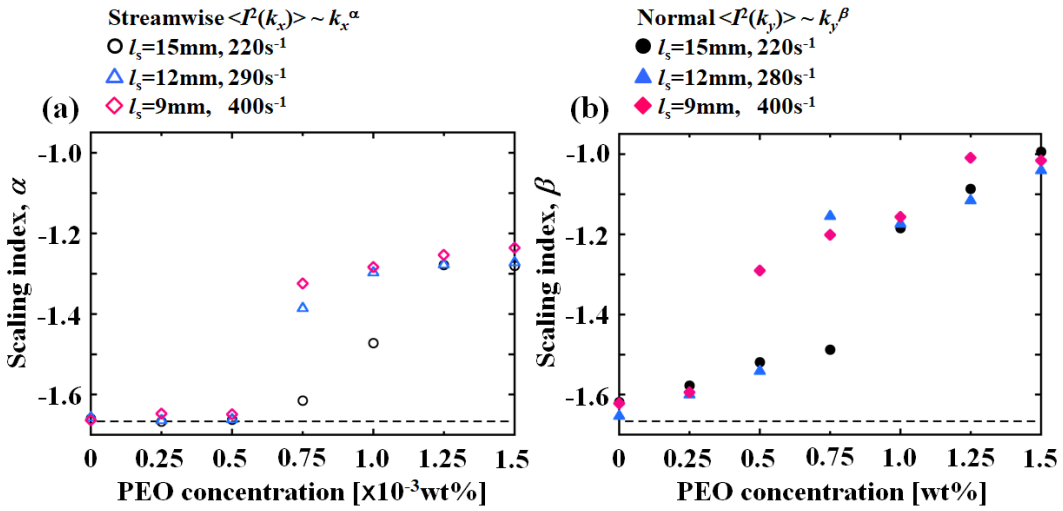

Fig. 8 Scaling index of power spectrum in (a) streamwise and (b) normal directions with different combs, namely l_s and $\dot{\varepsilon}$.

3.5. Velocity fields around comb

To clarify the energy transfer in 2D turbulent flow, the velocity fields close to the comb were observed and analyzed with PIV measurements. Figure 9 displays examples of instantaneous velocity vectors of the polymer-free solution and PEO solution around the comb of l_s = 12 mm. In the following turbulent statistical analysis, all the data are obtained with the comb of l_s = 12 mm. For the polymer-free solution, the velocity fluctuated widely in the normal direction close to the comb. Conversely, for the PEO solution, the local velocity fluctuation was diminished in the wake region. The velocity fluctuation in the normal direction gradually diminished with the distance from the grid. The vortices shed at the comb were merged and advected downstream; thus, the local velocity fluctuation approached a uniform mean velocity at the downstream.

Figure 10 displays the local velocity development in the streamwise direction with the distance from the grid. The horizontal axis denotes the normalized position in the normal direction. The position in the normal direction is normalized with the pitch of the cylinders. Thus, “0” in the horizontal axis in Fig. 10 corresponds to the center of the focussed cylinder. “1” in the axis corresponds to the center of the neighboring cylinder. The vertical axis in Fig. 10 indicates the mean local velocity in the streamwise direction, $\overline{U}_x$. The positive direction in the axis is downwards, which corresponds to the flow direction. $\overline{U}_x$ indicates a small value behind the cylinder. For the polymer-free solution, the $\overline{U}_x$ developed

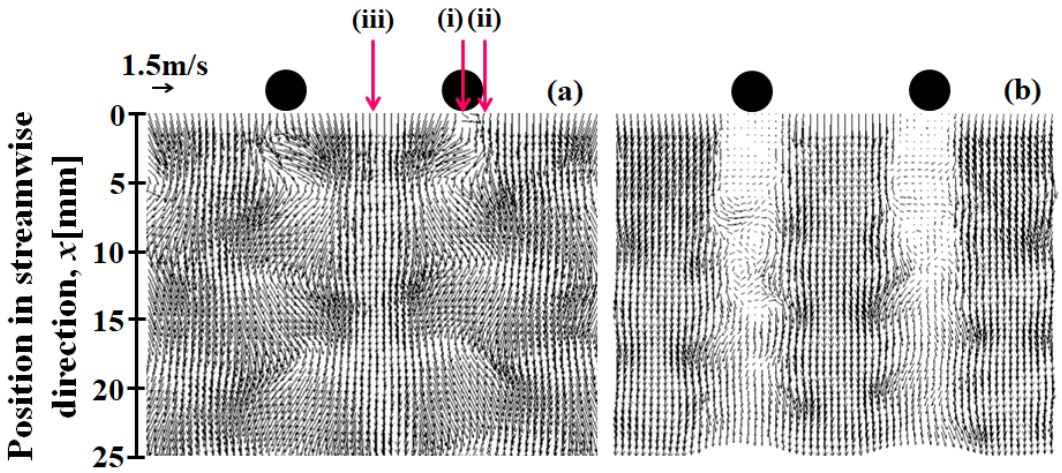

Fig. 9 Velocity fields of 2D turbulent flow of comb with l_s = 12 mm and $\dot{\varepsilon}$ = 290 s^{-1}. (a) Polymer-free solution and (b) PEO 1.5 × 10^{-3} wt% solution. The three arrows in (a) indicate the downstream positions in the normal direction where k, P, D, ε, and C, and the budget were calculated. The results are displayed in Figs. 11 and 12. Each position is called position (i), (ii), or (iii), which corresponds to the center of the cylinder, edge of the cylinder, or middle of the two cylinders, respectively.

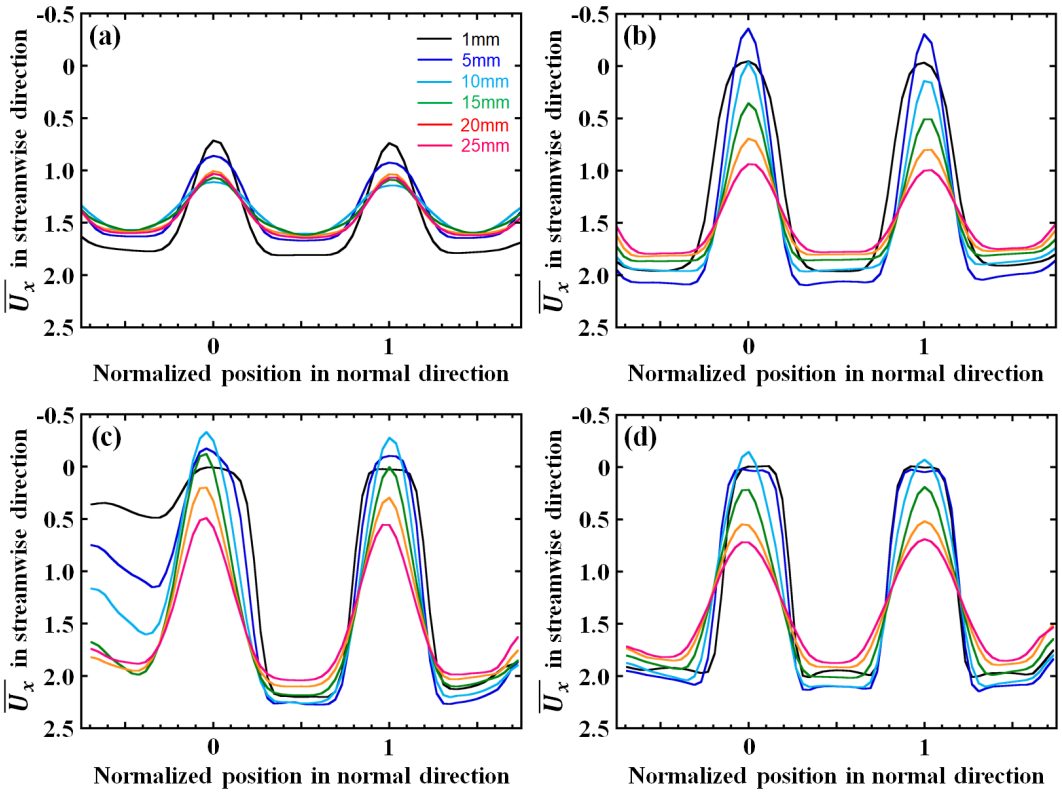

Fig. 10 Local mean velocity $\overline{U_x}$ development in streamwise direction at each downstream position. (a) Polymer-free solution, (b) PEO 0.5 × 10^{-3} wt%, (c) PEO 0.75 × 10^{-3} wt%, and (d) PEO 1.5 × 10^{-3} wt% solution.

quickly; thus, the difference in the velocity profiles of 1 mm to 25 mm downstream from the grind is small. The velocity difference in the normal direction was also relatively small. Conversely, for the PEO 0.5×10^{-3} wt% solution, the difference in the velocity profiles at each downstream and normal position is considerable. Moreover, PEO caused a negative velocity in the wake region within the formation length. The velocity field developed downstream, and the local velocity attained the mean velocity at a certain position from the grid.

3.6. Turbulent flow statistics

Based on the local velocity information obtained by PIV, the turbulent statistics of the 2D flow were calculated. Figure 11 displays the turbulent energy, k, development in the streamwise direction calculated by Eq. (1) with distance from the comb. In the figure, k is normalized by the streamwise mean velocity, U_m. The spacing of the comb is l_s = 12 mm, the position in the normal direction is located immediately behind the cylinder, at the edge of the cylinder, and in the middle of the two cylinders, as indicated in Fig. 9(a) as positions (i), (ii), and (iii). In the case of position (i), k was depressed immediately by adding PEO compared to the polymer-free solution. However, the reduction of k was not a one-way variation with the concentration of PEO. k was suppressed until the concentration of 0.5×10^{-3} wt%, and the value became extremely small at a concentration of 0.75×10^{-3} wt%. Subsequently, a characteristic peak again appeared at 1.0×10^{-3} wt%. For the PEO 0.5×10^{-3} wt% solution, the wake region expanded behind the cylinder; therefore, the distance from the comb to the position where k indicates the maximum value, $l_{k\text{-peak}}$ [m], became longer and the position was shifted downstream. For the 0.75×10^{-3} wt% solution, the vortices were virtually diminished close to the comb; therefore, the peak of k was extremely small and moved downstream. For the 1.0×10^{-3} wt% and 1.5×10^{-3} wt% solutions, the $l_{k\text{-peak}}$ became longer by increasing the concentration. In the case of position (ii), the tendency was similar to position (i), however the $l_{k\text{-peak}}$ was marginally shifted to the upper stream. Position “0” in the downstream direction in the streamwise direction starts at the lower edge of the cylinder. However, the flow separates from the edge of the cylinder, which is marginally in the upper position to “0”. Thus, the

$l_{\text{k-peak}}$ was marginally shifted to the upper position. In the case of position (iii), k was not observed.

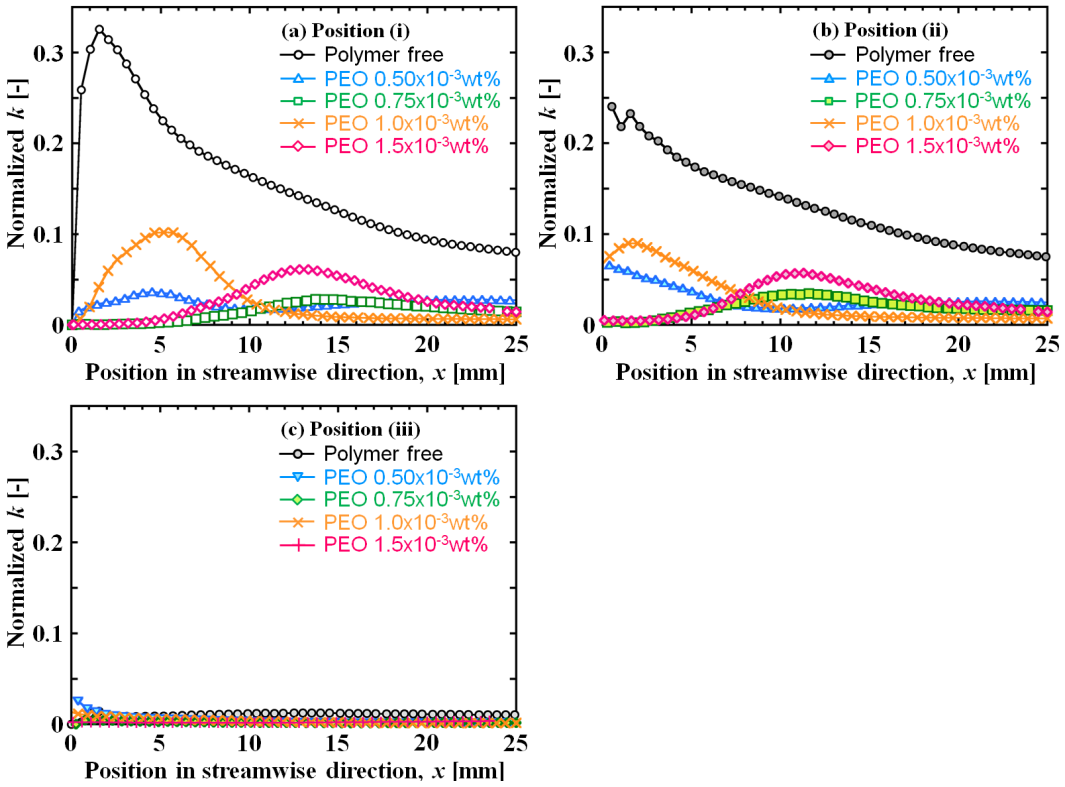

Fig. 11 Normalized k in each turbulent flow of each sample solution in the streamwise direction. (a) to (c) indicate normalized k at positions (i) to (iii), respectively.

To consider the origin of k, the values of P, D, and ε as described in Eqs. (3) to (5) of each solution were calculated. Figure 12 displays P, D, ε, and the budget of each sample solution in the streamwise direction at position (i). These values were normalized by the U_{m} and diameter of the cylinder. In the case of the polymer-free solution, the distance from the cylinder where the peak appeared in k, $l_{\text{k-peak}}$, and that in P were virtually the same. Thus, the k of the polymer-free solution originated from P in the turbulent flow. For the polymer solutions, as can be observed in Fig. 12, P, D, and ε of the PEO 0.5, 0.75, and 1.5×10^{-3} wt% solutions were negligible compared with that of the polymer-free solution. Whereas these values are virtually zero, a peak appears in the value of k. The peak observed in k is not explained by the turbulent energy transfer of Newtonian fluids. This implies that the peak value of k observed in the PEO solution originates from the polymer stress tensor, as described in Eq. (8). We assume that the value of k observed in the

polymer solution is related to instabilities caused by coil-stretch behavior and polymer elasticity; the origin of the value of k may be different from that of the Newtonian flow.

To confirm the accuracy of the measurements and calculations in the present study, the budget described in Eq. (7) is displayed in Fig. 12. In the case of the polymer-free solution, the budget was not close to zero in the wake region. This is a consequence of the three-dimensional disturbance of the flow. Here, the local velocities, U_i, in the streamwise and normal directions were measured and calculated by PIV. However, at the position immediately below the cylinder, the flow fluctuates in the spanwise direction. This fluctuation induces the budget. However, the budget converges to virtually zero 10 mm from the grid. In the case of the PEO solution, the difference was again negligible.

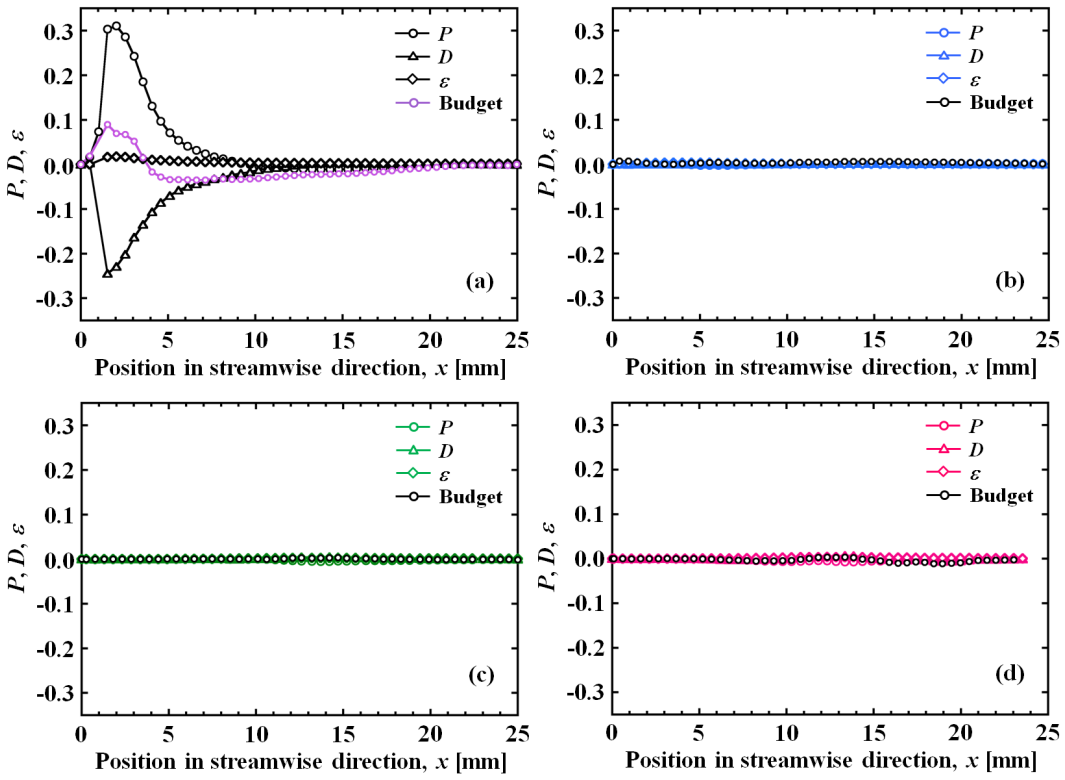

Fig. 12 Normalized P, D ε, and the budget of (a) polymer-free solution, (b) PEO 0.5×10^{-3} wt%, (c) PEO 0.75×10^{-3} wt%, and (d) PEO 1.5×10^{-3} wt% solution at position (i).

Here, we focus on the $l_{\text{k-peak}}$ that was shifted downstream with increasing PEO concentration. Hence, the $l_{\text{k-peak}}$ was divided by U_{vortex}, i.e., $l_{\text{k-peak}}/U_{\text{vortex}}$. The time scale obtained by the $l_{\text{k-peak}}/U_{\text{vortex}}$ was plotted against the concentration of each

solution. Subsequently, the $l_{k\text{-peak}}/U_{vortex}$ was compared to the relaxation time, as indicated in Fig. 13. There appeared to be a relationship between the values of the $l_{k\text{-peak}}/U_{vortex}$ of the 0.5, 1.0, and 1.5×10^{-3} wt% solutions and the relaxation time of each solution. However, in the case of the 0.75×10^{-3} wt% solution, the $l_{k\text{-peak}}/U_{vortex}$ characteristics are different from those of the others. In the case of the 0.5, 1.0, and 1.5×10^{-3} wt% solutions, the results imply that the polymers were extended at the cylinder and relaxed in the wake region; therefore, the first vortices appeared at a certain length, i.e., formation length. We assume that the mechanism is similar to the hibernation period proposed by Xi and Graham [15, 16]. As briefly described in the Introduction, Xi and Graham revealed that a highly extended polymer in turbulent flow induces the intermittent dynamics of viscoelastic turbulence [15, 16]. The degree of polymer stretching and drag reduction are temporally anti-correlated. The relationship between the degree of polymer extension in turbulent flow and turbulent flow structures has been extensively studied by Zhu et al. [20, 21]. The polymers stretch in active turbulence and induce the following weak turbulent flow. In the present study, polymers stretched at the cylinder, thereby expanding the wake region. Subsequently, polymers relaxed in the wake region, and then, the first vortex appeared after the formation length. As observed in the experiments, it was assumed that the macroscopic vortices were influenced by the extended polymers and their relaxation time in the microscale. Therefore, k increased without P in the polymer solution. As shown in Fig. 13, $l_{k\text{-peak}}/U_{vortex}$ increased with the relaxation time of each solution. The slope of $l_{k\text{-peak}}/U_{vortex}$ against the solution concentration is less than that of the relaxation time; quantitative analysis of the slope should be the next step.

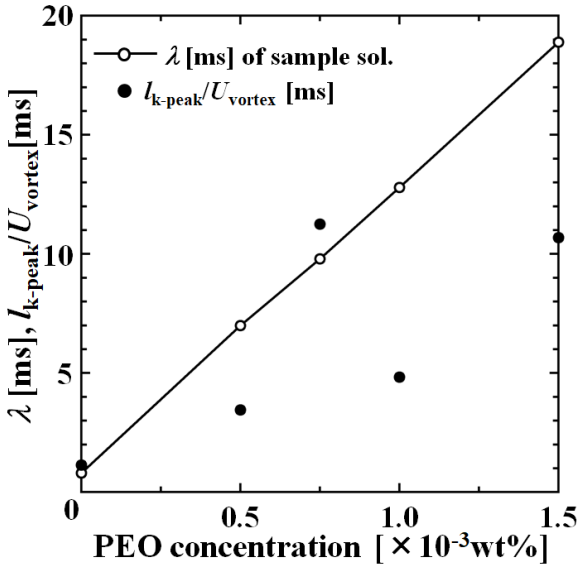

Fig. 13 Comparison of time scale of λ and $l_{k\text{-}peak}/U_{vortex}$.

4. Conclusion

An experimental study was performed to investigate the effects of the extensional rheological properties of polymer solutions on vortex shedding in 2D turbulent flow and on turbulent statistics. The mean extensional rate was varied by changing the spacing of the cylinders of the combs that induced turbulent flow. The main conclusions of this study are as follows.

1. Vortex shedding at the cylinder of each comb was visualized through interference patterns. The vortices shed at the cylinder were categorized into three types. The original vortices were categorized as Vortex-Type1. The wake region, i.e., formation length expanded by increasing the PEO concentration. Subsequently, the vortices were virtually diminished, and the transition regime was called Vortex-Type2. The transition regime was shifted to a reduced concentration by increasing the mean extensional rate. The vortices called Vortex-Type3 then appeared when the concentration was further increased. Vortex shedding was quantified by the shedding frequency, that is, *St*. *St* was not a one-direction variation in the PEO concentration.

2. The vortex shedding regimes were influenced by the extensional relaxation time of each solution measured by a CaBER. The relationship between the relaxation time and period of vortex shedding, $1/f$, at the comb defined the vortex

flow regimes, as Vortex-Type1, 2, and 3. The finding was valid for all vortices shed at different combs that induced different mean extensional rates.

3. The scaling index of the power spectrum of the 2D turbulent flow was calculated. The scaling index indicated that the energy transfer in the 2D flow was varied at a certain concentration. The concentration was reduced by increasing the mean extensional rate, which corresponded to the concentration at which Vortex-Type2 was observed.

4. The velocity fields behind the comb were measured by PIV, and the turbulent statistics were calculated. The turbulent energy k behind the cylinder was plotted to the distance from the cylinder. k was suppressed by adding PEO, and was virtually diminished at the concentration where Vortex-Type2 was observed. Subsequently, k was again increased by increasing the PEO concentration, and a characteristic peak appeared downstream. However, the increase in k in the polymer solution was not explained by the production, P, diffusion, D, and dissipation, ε, calculated by the equation based on Newtonian fluids. Indeed, P, D, and ε were negligible. The value of k observed in the polymer solution may be related to the instability caused by the coil-stretch behavior and polymer elasticity.

5. Although the slope of $l_{\text{k-peak}}/U_{\text{vortex}}$ versus solution concentration in the flow regime of Vortex-Type1 and Vortex-Type3 was less than that of the relaxation time, there appeared to be a relationship between $l_{\text{k-peak}}/U_{\text{vortex}}$ and relaxation time. The results imply that the polymers were extended at the cylinder and gradually relaxed in the wake region. Therefore, the first vortex appeared after the formation length, which induced k without P. It seems that the mechanism is similar to the relationship between the hibernation period and polymer relaxation process in polymer-doped turbulent flows.

Acknowledgements

The present study was supported in part by a Grant-in-Aid for Scientific Research (B) (Project No.: 19H02497) and a Challenging Research (Exploratory) (Project No.: 19K22083) from the Japan Society for the Promotion of Science (JSPS KAKENHI).

Reference

[1] P.S. Virk, E.W. Merrill, H.S. Mickley, K.A. Smith, E.L. Mollo-Christensen, The Toms phenomenon: turbulent pipe flow of dilute polymer solutions, J. Fluid Mech. 30 (1967) 305–328

[2] F.T. Pinho, J.H. Whitelaw, Flow of non-Newtonian fluids in a pipe, J. Non-Newtonian Fluid Mech. 34 (1990) 129–144.

[3] M.P. Escudier, A.K. Nickson, R.J. Poole, Turbulent flow of viscoelastic shear-thinning liquids through a rectangular duct: Quantification of turbulence anisotropy, J. Non-Newtonian Fluid Mech. 160 (2009) 2–10.

[4] Z. Fu, T. Otsuki, M. Motozawa, T. Kurosawa, B. Yu, Y. Kawaguchi, Experimental investigation of polymer diffusion in the drag-reduced turbulent channel flow of inhomogeneous solution, Int. J. Heat and Mass Trans. 77 (2014) 860–873.

[5] M. Motozawa, T. Sawada, S. Ishitsuka, K. Iwamoto, H. Ando, T. Senda, Y. Kawaguchi, Experimental investigation on streamwise development of turbulent structure of drag-reducing channel flow with dosed polymer solution from channel wall, Int. J. Heat and Fluid Flow 50 (2014) 51–62.

[6] C.H. Hong, C.H. Jang, H.J. Choi, Turbulent drag reduction with polymers in rotating disk flow, Polymers 7 (2015) 1279–1298.

[7] T. Wei, W.W. Willmarth, Modifying turbulent structure with drag-reducing polymer additives in turbulent channel flows, J. Fluid Mech. 245 (1992) 619–641.

[8] J.M.J. den Toonder, F.T.M. Nieuwstadt, G.D.C. Kuiken, The role of elongational viscosity in the mechanism of drag reduction by polymer additives, Appl. Scient. Res. 54 (1995) 95–123.

[9] J.M.J. den Toonder, M.A Hulsen, G.D.C. Kuiken, F.T.M. Nieuwstadt, Drag reduction by polymer additives in a turbulent pipe flow: numerical and laboratory experiments, J. Fluid Mech. 337 (1997) 193–231.

[10] J.L. Lumley, Drag reduction in turbulent flow by polymer additives, J. Polym. Sci. Macromol. Rev. 7, (1973) 263–290.

[11] T. Min, J.Y. Yoo, H. Choi, D.D. Joseph, Drag reduction by polymer additives in a turbulent channel flow, J. Fluid Mech. 486 (2003) 213–238.

[12] B.E. Owolabi, D.J.C. Dennis, R.J. Poole, Turbulent drag reduction by polymer additives in parallel-shear flows, J. Fluid Mech. 827 (2017) R4–1–12.

[13] C. Wagner, Y. Amarouchene, P. Doyle, D. Bonn, Turbulent-drag reduction of polyelectrolyte solutions: Relation with the elongational viscosity, Europhys. Lett. 64 (2003) 823–829.

[14] Y. Amarouchene, D. Bonn, H. Kellay, T.-S. Lo, V.S. L'vov, I. Procaccia, Reynolds number dependence of drag reduction by rodlike polymers, Phys. Fluids 20 (2008) 065108–1–8.

[15] L. Xi, M.D. Graham, Active and hibernating turbulence in minimal channel flow of Newtonian and polymeric fluids, Phys. Rev. Lett. 104 (2010) 218301–1–4.

[16] M.D. Graham, Drag reduction and the dynamics of turbulence in simple and complex fluids, Phys. Fluids 26 (2014) 101301–1–24.

[17] R.D. Whalley, D.J.C. Dennis, M.D. Graham, R.J. Poole, An experimental investigation into spatiotemporal intermittencies in turbulent channel flow close to transition, Exper. Fluids 60 (2019) 102–1–16.

[18] S.-N. Wang, A. Shekar, M.D. Graham, Spatiotemporal dynamics of viscoelastic turbulence in transitional channel flow, J. Non-Newtonian Fluid Mech. 244 (2017) 104–122.

[19] A. Kushwaha, J.S. Park, M.D. Graham, Temporal and spatial intermittencies within channel flow turbulence near transition, Phys. Rev. Fluids 2 (2017) 024603–1–30.

[20] L. Zhu, H. Schrobsdorff, T.M. Schneider, L. Xi, Distinct transition in flow statistics and vortex dynamics between low- and high-extent turbulent drag reduction in polymer fluids, J. Non-Newtonian Fluid Mech. 262 (2018) 115–130.

[21] L. Zhu, X. Bai, E. Krushelnycky, L. Xi, Transient dynamics of turbulence growth and bursting: Effects of drag-reducing polymers, J. Non-Newtonian Fluid Mech. 266 (2019) 127–142.

[22] O. Cadot, M. Lebey, Shear instability inhibition in a cylinder wake by local injection of a viscoelastic fluid, Phys. Fluids 11 (1999) 494–496.

[23] O. Cadot, S. Kumar, Experimental characterization of viscoelastic effects on two- and three-dimensional shear instabilities, J. Fluid Mech. 416 (2000) 151–172.

[24] H. Usui, T. Shibata, Y. Sano, Kármán vortex behind a circular cylinder in dilute polymer solutions, J. Chem. Eng. Jpn. 13 (1980) 77–79.

[25] M. Sahin, R.G. Owens, On the effects of viscoelasticity on two-dimensional vortex dynamics in the cylinder wake, J. Non-Newtonian Fluid Mech. 123 (2004) 121–139.

[26] P.M. Coelho, F.T. Pinho, Vortex shedding in cylinder flow of shear-thinning fluids I. Identification and demarcation of flow regimes, J. Non-Newtonian Fluid Mech. 110 (2003) 143–176.

[27] P.M. Coelho, F.T. Pinho, Vortex shedding in cylinder flow of shear-thinning fluids II. Flow characteristics, J. Non-Newtonian Fluid Mech. 110 (2003) 177–193.

[28] P.M. Coelho, F.T. Pinho, Vortex shedding in cylinder flow of shear-thinning fluids. III Pressure measurements, J. Non-Newtonian Fluid Mech. 121 (2004) 55–68.

[29] P.J. Oliveira, Method for time-dependent simulations of viscoelastic flows: vortex shedding behind cylinder, J. Non-Newtonian Fluid Mech. 101 (2001) 113–137.

[30] P.J. Oliveira, A.I.P. Miranda, A numerical study of steady and unsteady viscoelastic flow past bounded cylinders, J. Non-Newtonian Fluid Mech. 127 (2005) 51–66.

[31] Y.L. Xiong, C.H. Bruneau, H. Kellay, Drag enhancement and drag reduction in viscoelastic fluid flow around a cylinder, EPL. 91 (2010) 64001–p1–p6.

[32] Y.L. Xiong, C.H. Bruneau, H. Kellay, A numerical study of two dimensional flows past a bluff body for dilute polymer solutions, J. Non-Newtonian Fluid Mech. 196 (2013) 8–26.

[33] N. François, D. Lasne, Y. Amarouchene, B. Lounis, H. Kellay, Drag enhancement with polymers, Phys. Rev. Lett. 100 (2008) 018302–1–4.

[34] Y. Asano, H. Watanabe, H. Noguchi, Polymer effects on Kármán vortex: Molecular dynamics study, J. Chem. Phys. 148 (2018) 144901–1–9.

[35] H. Kellay, W.I. Goldburg, Two-dimensional turbulence: a review of some recent experiments, Rep. Prog. Phys. 65 (2002) 845–894.

[36] G. Boffetta, R.E. Ecke, Two-dimensional turbulence, Annu. Rev. Fluid Mech. 44 (2012) 427–51.

[37] M.A. Rutgers, X-L. Wu, R. Bhagavatula, A.A. Petersen, W.I. Goldburg, Two-dimensional velocity profiles and laminar boundary layers in flowing soap films, Phys. Fluids 8 (1996) 2847–2854.

[38] R. Hidema, H. Suzuki, S. Hisamatsu, Y. Komoda, H. Furukawa, Effects of the extensional rate on two-dimensional turbulence of semi–dilute polymer solution flows, Rheol. Acta 52 (2013) 949–961.

[39] R. Hidema, H. Suzuki, S. Hisamatsu, Y. Komoda, Characteristic scales of two-dimensional turbulence in polymer solutions, AIChE J. 60 (2014) 1854–1862.

[40] R. Hidema, H. Suzuki, I. Murao, S. Hisamatsu, Y. Komoda, Effects of extensional rates on anisotropic structures and characteristic scales of two-dimensional turbulence in polymer solutions, Flow Turbul. Combust. 96 (2016) 227–244.

[41] R. Hidema, I. Murao, Y. Komoda, H. Suzuki, Effects of the extensional rheological properties of polymer solutions on vortex shedding and turbulence characteristics in a two-dimensional turbulent flow, J. Non-Newtonian Fluid Mech. 254 (2018) 1–11.

[42] G.H. McKinley, A. Tripathi, How to extract the Newtonian viscosity from capillary breakup measurements in a filament rheometer, J. Rheol. 44 (2000) 653–670.

[43] S.L. Anna, G.H. McKinley, Elasto-capillary thinning and breakup of model elastic liquids, J. Rheol. 45 (2001) 115–138.

[44] L.R. Rodd, T.P. Scott, J.J. Cooper-White, G.H. McKinley, Capillary break-up rheometry of low-viscosity elastic fluids, Appl. Rheol. 15 (2005) 12–27.

[45] M. Rivera, P. Vorobieff, R.E. Ecke, Turbulence in flowing soap films: Velocity, vorticity, and thickness fields, Phys. Rev. Lett. 81 (1998) 1417–1420.